

Article

Development of Visible Multi–Bandpass Filter Based on F–P Structure

Hongyan Jiang¹, Rongwei Fan¹, Yiqin Ji^{1,2}, Kai Guo³, Shifu Xiong⁴, Bing Sun⁵, Chen Zhang², Xing Wang¹ and Deying Chen^{1,*}

¹ National Key Laboratory of Science and Technology on Tunable Laser, Harbin Institute of Technology, Harbin 150080, China; jhy_optics@126.com (H.J.); rwan@hit.edu.cn (R.F.); ji_yiqin@163.com (Y.J.)

² Tianjin Jinhang Technical Physics Institute, Tianjin 300080, China

³ Optoelectric Component Research and Development Center, Beijing Institute of Control Engineering, Beijing 100094, China; kg_optics@126.com

⁴ Tianjin Key Laboratory of Functional Crystal Materials, Institute of Functional Crystals, Tianjin University of Technology, Tianjin 300384, China

⁵ Academy of Opto–Electronics, China Electronics Technology Group Corporation, Tianjin 300308, China; sunbing_optics@126.com

* Correspondence: dychen@hit.edu.cn

Abstract: In order to reduce the noise interference of smart wearable devices, spectral filtering technology is used to suppress noise. This technology prevents interference signals from entering the detector from the source, thereby achieving high–precision noise reduction processing. According to the system requirements, a multi–bandpass filter with a wavelength range of 400~1000 nm was designed and prepared on a BK7 substrate. Ta₂O₅ and SiO₂ were selected as the high– and low–refractive–index materials, respectively. By analyzing the –Fabry–Perot narrowband theory, the bandwidth matching coefficient was computed, and the interference order was calculated using the interval of the transmission peak wavelengths. Multiple F–P coating systems were connected through the matching layer to adjust the position of the transmission peak and broaden the bandwidth range. The design was optimized using Macloed film system design software, resulting in the design of a wide half–wave and cutoff multi–bandpass filter. The appropriate preparation process was chosen based on changes in refractive index, surface roughness, and the temperature gradient of the materials. The filter was then produced using Leybold SYRUSpro1110. Sensitivity, filter roughness, and the weak absorption of the film system were tested, and the results met the system requirements.

Keywords: smart wearables; signal noise; spectral filtering; multiband bandpass



Citation: Jiang, H.; Fan, R.; Ji, Y.; Guo, K.; Xiong, S.; Sun, B.; Zhang, C.; Wang, X.; Chen, D. Development of Visible Multi–Bandpass Filter Based on F–P Structure. *Coatings* **2023**, *13*, 1341. <https://doi.org/10.3390/coatings13081341>

Academic Editor: Andrey V. Osipov

Received: 29 May 2023

Revised: 14 July 2023

Accepted: 27 July 2023

Published: 30 July 2023



Copyright: © 2023 by the authors. Licensee MDPI, Basel, Switzerland. This article is an open access article distributed under the terms and conditions of the Creative Commons Attribution (CC BY) license (<https://creativecommons.org/licenses/by/4.0/>).

1. Introduction

Smart wearable devices can monitor human physiological parameters (biological indicators) in real–time and manage health better [1,2]. A sensor serves as the forefront of smart wearable devices, directly collecting the user’s biological information and then sending it to the data processing section for processing [3]. Photoplethysmography (PPG) [4,5] involves the use of photoplethysmography technology to detect human physiological parameters. The sensor includes a photodiode (PD) and a light–emitting diode (LED). There are two types of PPG sensors, transmission [6] and reflection [7,8] sensors, and the reflection type is commonly used in wearable devices. The light emitted by the LED is reflected by human blood and tissues and then received by the PD. By detecting the differences in the reflected light intensity after being absorbed by human blood and tissues, human physiological parameters are recorded.

When PPG sensors are installed on the user's watches, they can be affected by various internal and external noise sources [9,10], including interference caused by the movement of the measurement position, natural light, and fluorescent lighting. Therefore, the data need to undergo various filtering processes. In particular, interference from environmental light can enter the PD detector through the gap between the skin and the PPG sensor. To address this issue, it is necessary to filter the received interference signals using digital signal processing filtering algorithms [11,12]. However, due to limitations such as sampling frequency and signal processing algorithms, it is challenging to completely eliminate the interference signal. This can impact the signal-to-noise ratio of the detector and lead to measurement errors in human physiological parameters.

For the PPG sensor, it is desirable to only receive signals related to the LED light source, while other unrelated signals are considered interference noise. However, since the PD detector receives a wide spectral band, in addition to receiving LED light, it will also receive all light from 400~1000 nm. We propose a multi-bandpass filter structure that can only allow a LED light source to pass through in the direction of the detector, preventing interference signals from entering the detector at source and achieving high-precision noise reduction processing.

The problem of PPG only receiving relevant signals can be solved by using the spectral filtering method, which is achieved by multiple layers of optical thin film [13]. There have been many design solutions for multi-bandpass filters in recent years. In 2003, Li Wang et al. designed a multi-bandpass filter at 487 nm, 550 nm, and 632 nm by selecting different materials and changing the thickness of the spacing layer [14], but the half-wave width was narrow. In 2006, Shaowei Wang et al. used a combination of etching methods to obtain multiple single-channel optical filters, but the structure was complex and the process was difficult [15]. In 2008, Kamikawa used a shared mirror to form a rectangular-shaped passband with good passband width [16], but the distance between the two passbands could not be designed to be very wide. In 2018, Shuaifeng Zhao et al. fabricated a dual-pass fluorescence filter with 561 nm and 687 nm wavelengths using a single-substrate double-sided coating structure [17]. In 2019, Yuanqiang Zhu designed a three-channel optical filter at 480 nm, 550 nm, and 644 nm by increasing the interference order and improving the reflectivity on both sides [18], but the half-wave width was narrow. In 2020, Gang Chen et al. prepared a dual-bandpass thin film filter for both visible light and near-infrared by depositing dielectric films on both surfaces of the substrate [19]. In 2021, Shun Zhou et al. fabricated a dual-channel bandpass thin film-filter for the mid-infrared region using the lift-off process. However, the lift-off process techniques are complex [20]. In 2020, Shaopeng Ren et al. proposed a design method based on a cyclic nesting model. They calculated the adjustment factor of the peak position and bandwidth matching coefficient and designed a multi-pass filter at 455 nm, 530 nm, and 631 nm for fluorescence detection [21], but the spectral range was not wide enough. Therefore, we aim to design a multi-bandpass filter with a wide half-wave and cutoff. We need to ensure transmission in three spectral bands: 515~545 nm, 645~675 nm, and 925~955 nm. By calculating the interference order of the film system based on the transmission peak wavelength interval of the narrowband filter, and coupling multiple F-P structures, a multi-bandpass filter with a wavelength range of 400~1000 nm is designed. The unnecessary spectral bands can be suppressed, and the required spectral bands can be passed through, allowing PPG to only receive the desired signals and filter unnecessary noise.

2. Design of Multi-Bandpass Filter

The specific parameter requirements for the multi-bandpass filter are shown in Table 1.

Table 1. Technical parameters of multi–bandpass filter.

Parameter	Specification
Angle	0°~30°
Transmission band/nm	515~545, 645~675 and 925~955
Transmittance/%	≥90
Waveband of cut–off region/nm	450~490, 565~625 and 700~900
Transmissivity of cut–off region/%	<1
Filter size/mm	Φ14.6
Filter thickness/mm	2
RMS/nm	<0.05
Weak absorption/ppm	<200

2.1. Theoretical Design of Multi–Bandpass Filter

The design methods for multi–bandpass filter membranes include multi–membrane combinations [19,22], a guided–mode resonance filter [23], and membrane designs based on the F–P structure. The F–P structure design methods include increasing the interference order [18], serially connecting multiple F–P cavities [16], and adjusting the bandwidth matching coefficient [24,25], which can adjust the passband position and passband width of the basic membrane system. However, due to material’s refractive index limitations, the phase shift of reflection on both sides of the center wavelength is fixed, and can only be designed within the width range of the cutoff band, making it impossible to design a multi–bandpass filter with wider ranges. We aim to design a multi–bandpass filter with wide a half–wave, wide passband intervals, and long spectral ranges. Based on the Fabry–Perot narrowband theory [26], we propose using the transmission sub–peaks that appear on both sides of the main peak at the center wavelength of the narrowband filter for design. The filter is designed by overlapping multiple F–P cavity structures.

In the F–P structure filter, for a certain membrane system, the characteristic matrix is [27]

$$\begin{bmatrix} B \\ C \end{bmatrix} = \begin{bmatrix} M_{11} & iM_{12} \\ iM_{21} & M_{22} \end{bmatrix} \begin{bmatrix} 1 \\ n_g \end{bmatrix} \quad (1)$$

Then, the phase shift, φ , of the reflection for multiple layers is

$$\tan \varphi = \frac{2n_0n_gM_{12}M_{22} - 2n_0M_{11}M_{21}}{n_0^2M_{11}^2 - n_g^2M_{22}^2 + n_0^2n_g^2M_{12}^2 - M_{21}^2} \quad (2)$$

where n_0 and n_g are the refractive indices of the incident medium and the substrate.

When the admittance on both sides of the intermediate layer is the same, the transmittance of the filter [20] is

$$T = \frac{T_1 \cdot T_2}{(1 - \sqrt{R_1 \cdot R_2})^2} \cdot \frac{1}{1 + F \sin^2 \frac{1}{2}(\varphi_1 + \varphi_2 - 2\delta)} \quad (3)$$

$$F = \frac{4\sqrt{R_1 \cdot R_2}}{(1 - \sqrt{R_1 \cdot R_2})^2} \quad (4)$$

$$\delta = \frac{2\pi nd}{\lambda} \quad (5)$$

where T_1 , T_2 , R_1 and R_2 are the transmittance and reflectance of the reflective film system on both sides of the spacer layer, and φ_1 and φ_2 are the reflection phase shifts of the reflective film system on both sides.

The center wavelength corresponding to the maximum transmittance of the filter film is

$$\phi = \frac{\varphi_1 + \varphi_2}{2} - \frac{2\pi nd}{\lambda} = m\pi, m = 0, \pm 1, \pm 2 \dots \quad (6)$$

$$\frac{1}{\lambda} = \frac{1}{2nd} \left(\frac{\varphi_1 + \varphi_2}{2\pi} - m \right) \quad (7)$$

where m is the interference order, and $m = k + \frac{(\varphi_1 + \varphi_2)}{2\pi}$, ($k = 0, 1, 2, \dots$)

The channel half-width corresponding to the central wavelength is

$$\Delta\lambda_{0.5} = \frac{2\lambda_0}{m\pi} \arcsin \left(\frac{(1 - \sqrt{R_1 R_2})}{2 \cdot \sqrt[4]{R_1 R_2}} \right) \quad (8)$$

Increasing the interference order will result in the occurrence of several transmission side lobes on both sides of the main peak of the central wavelength, and the wavelength spacing of these transmission side lobes is as follows:

$$\Delta\lambda = \lambda_m - \lambda_{m+1} = \frac{2nd}{m(m+1)} = \frac{\lambda_0}{m+1} \quad (9)$$

According to Equation (6), the interference order can be calculated as follows:

$$m = \left(\frac{\lambda_0}{\Delta\lambda} \right) - 1 \quad (10)$$

When the center wavelength of a narrow-band filter is determined, fixed reflection bands appear on both sides of it. The bandwidth of the reflection band is only related to the refractive index of the filter material, and the bandwidth of the reflection band is $2\Delta g$, so,

$$\Delta g = \frac{2}{\pi} \sin^{-1} \left(\frac{n_H - n_L}{n_H + n_L} \right) \quad (11)$$

where n_H is the high-refractive-index material's refractive index; n_L is the low-refractive-index material's refractive index.

After determining the width of the reflective band, the position of the second peak can be determined. The high-reflection region, expressed in terms of relative wave number, Δg , is between $1 + \Delta g$ and $1 - \Delta g$, and the corresponding wavelength range is as follows:

$$\lambda_1 = \frac{\lambda_0}{1 + \Delta g}, \quad \lambda_2 = \frac{\lambda_0}{1 - \Delta g} \quad (12)$$

The wavelength width of the high reflection band is as follows:

$$\Delta\lambda = \frac{\lambda_0}{1 - \Delta g} - \frac{\lambda_0}{1 + \Delta g} \approx 2\Delta g\lambda_0 \quad (13)$$

The wavelength width between the main peak and the side lobes is approximately $\Delta g\lambda_0$.

According to the requirements of the spectrum, Ta_2O_5 and SiO_2 were selected as high- and low-refractive-index materials, respectively. Ta_2O_5 has a transparent region of 0.35~10 μm , with a high refractive index and low absorption [28,29]. SiO_2 has a transparent region of 0.2~9 μm , with good optical and chemical stability. In addition, Ta_2O_5 and SiO_2 match well, so Ta_2O_5 and SiO_2 were chosen as high- and low-refractive-index materials, respectively.

According to Equation (2), when the reflectivity of the mirrors at both ends of the F-P structure is determined, the wavelength-dependent phase shift, φ , for reflection is fixed, and the reflection range cannot be designed to be very wide. As the wavelength intervals between the 515~545 nm and 645~675 nm bands are relatively small, the first and second passbands should be designed first.

The basic structure of the dual bandpass membrane system is Sub | (aHbL)^m 2H (bLaH)^s | Air, where Sub represents the substrate, H represents the high-refractive-index

material Ta_2O_5 , L represents the low–refractive–index material, SiO_2 , a and b are bandwidth matching coefficients, s is the number of cycles of the reflective membrane stack, and m is the interference order. The values of a , b , and s determine the bandwidth of the passband, while m determines the number and relative position of the passbands. The center wavelength is 580 nm. According to the spectral curve changes in Figure 1a–c, it is analyzed that, as a and b increase, the passband becomes wider, but the cutoff becomes worse; s can increase the number of passbands and narrow the bandwidth; and as m increases, the spacing between passbands becomes smaller. Based on the target wavelength, appropriate parameter values can be calculated. According to Equation (9), in order to design a dual–band membrane system structure with center wavelengths of 530 nm and 660 nm, with $\Delta\lambda = 130$ nm and $\lambda_0 = 580$ nm, it can be calculated that $m = 3.5$. By simulating the required half–wavelength, it can be obtained that $a = 1$, $b = 1$, and $s = 2$. The final determined dual–band film structure is $Sub | (HL)^2 7H (LH)^2 | Air$. We obtained the transmission curve shown in Figure 1d.

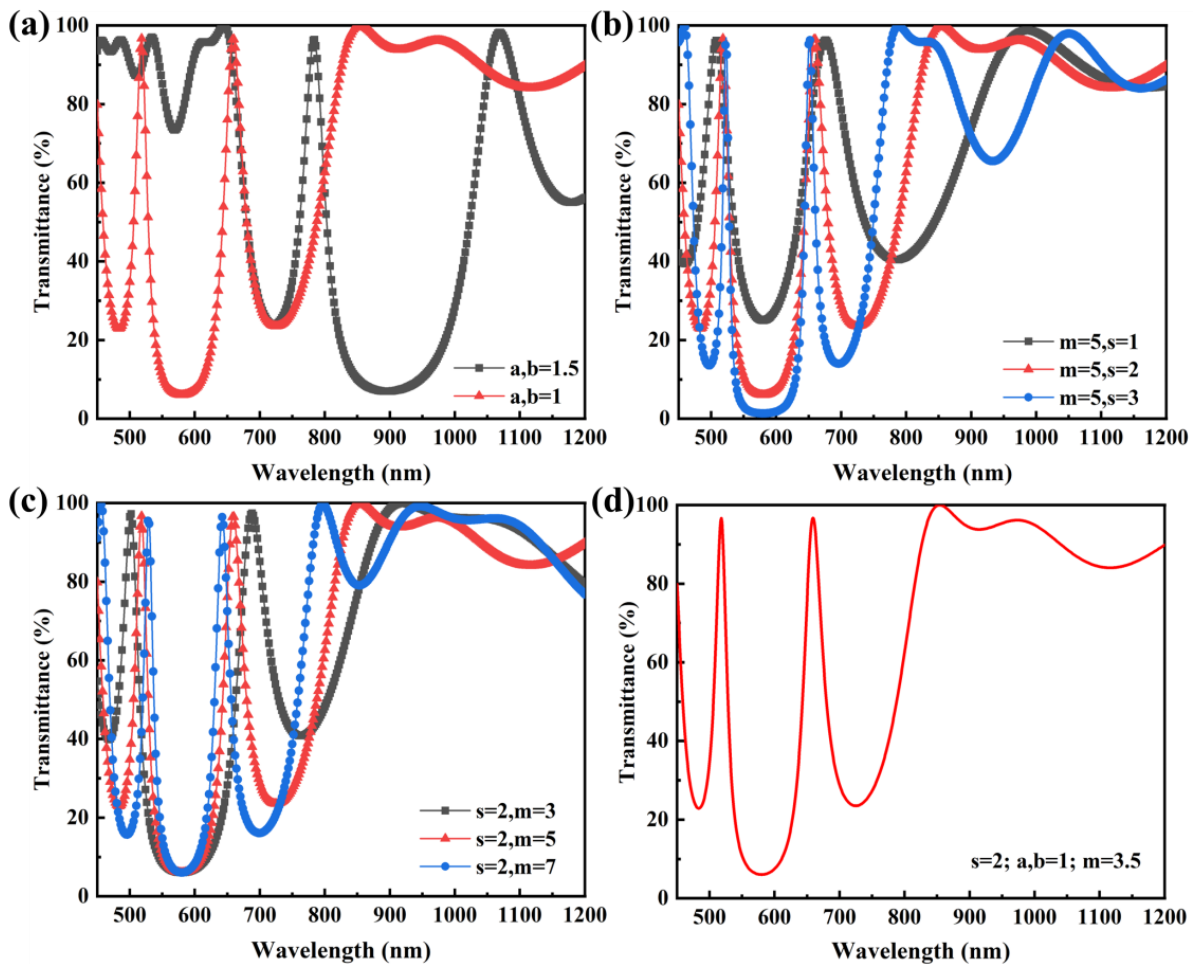


Figure 1. (a) Transmittance curves of bandwidth matching coefficients a , $b = 1$ and a , $b = 1.5$ with the number of film layer periods of $s = 2$ and the interference order $m = 5$. (b) Transmittance curves of bandwidth matching coefficients a , $b = 1$ and interference order $m = 5$ for film layer periods $s = 1, 2$, and 3 . (c) Transmittance curves of interference orders $m = 3, 5$, and 7 for film layer periods of $s = 2$ and the bandwidth matching coefficient a , $b = 1$. (d) Transmittance curve of dual–band filter.

By coupling multiple F–P structures and connecting them with a matching layer, L, the passband spectrum range is widened. Based on a dual–bandpass membrane system in Figure 1d, an additional F–P structure is overlaid and connected by a matching layer, L, with the basic structure being $Sub | (HL)^2 7H (LH)^2 L n(HL)^2 2H (LH)^2 | Air$. By adjusting

the coefficient, n , the initial membrane system has a basic shape of three transmission peaks, and $n = 1.62$ is obtained after multiple simulations. The transmission curve shown in Figure 2 has three basic shapes of transmission peaks in the wavelength bands of 515~545 nm, 645~675 nm, and 925~955 nm.

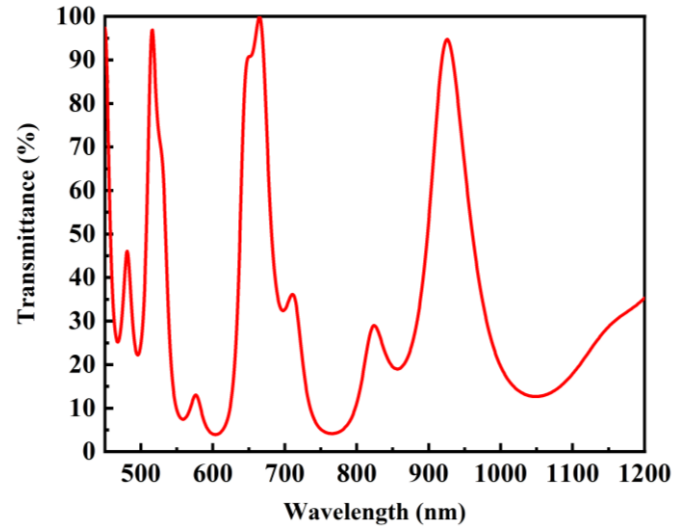


Figure 2. Transmittance curve of basal membrane system.

2.2. Optimize Design

Figure 2 presents the basic prototype of a multi-bandpass filter. Based on this prototype, optimization was carried out using the Simplex, Optimac, and Needle Synthesis methods in the Macleod film design software [30]. The optimized film structure is as follows: Sub | 0.92H 1.61L 0.82H 0.11L 0.13H 1.22L 1.26H 0.18L 0.12H 1.16L 0.78H 0.44L | Air. There was a reference wavelength of 580 nm, a total of 84 layers, and a physical thickness of about 9.357 μm . The theoretical 3D design curve of the transmittance is shown in Figure 3.

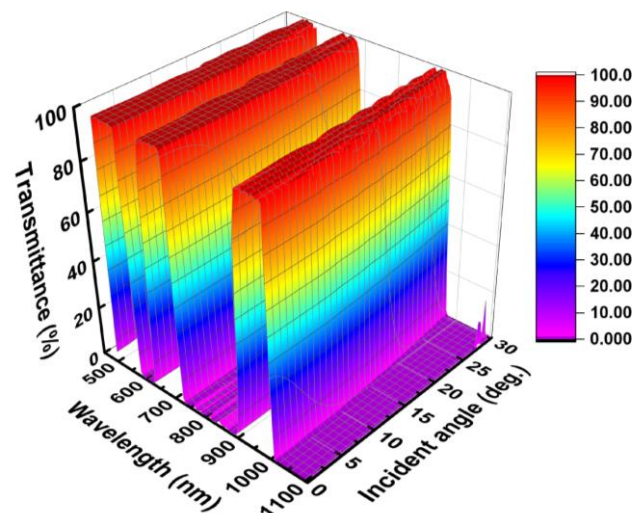


Figure 3. Theoretical design curve of multi-bandpass filter (3D).

The average transmittance under 0°, 10°, 20° and 30° conditions are shown in Table 2, and this design can meet the usage requirements.

Table 2. Design parameters of multi–bandpass filter.

Incident Angle	Wavelength/nm	Average Transmittance/%
0°	515~545	99.80
	645~675	99.69
	925~955	99.11
10°	515~545	99.78
	645~675	99.68
	925~955	99.23
20°	515~545	99.68
	645~675	99.62
	925~955	99.19
30°	515~545	98.54
	645~675	99.10
	925~955	95.63

2.3. Sensitivity Analysis

The design of a multi–bandpass filter has the advantages of a wide half–wave, deep background, and high cutoff. The design avoids ultra–thin layers, reducing errors during the manufacturing process. The filter demonstrates good stability and reproducibility, meeting the requirements for spectral design and facilitating easier and more reliable production. Sensitivity analysis is an important indicator for evaluating the accuracy and reliability of film preparation [31]. Using Essential Macleod software, tolerance simulations were performed with a random error of 3‰ 20 times. The simulation results are shown in Figure 4, with minimal waveform variations, which fulfill system design and manufacturing requirements better.

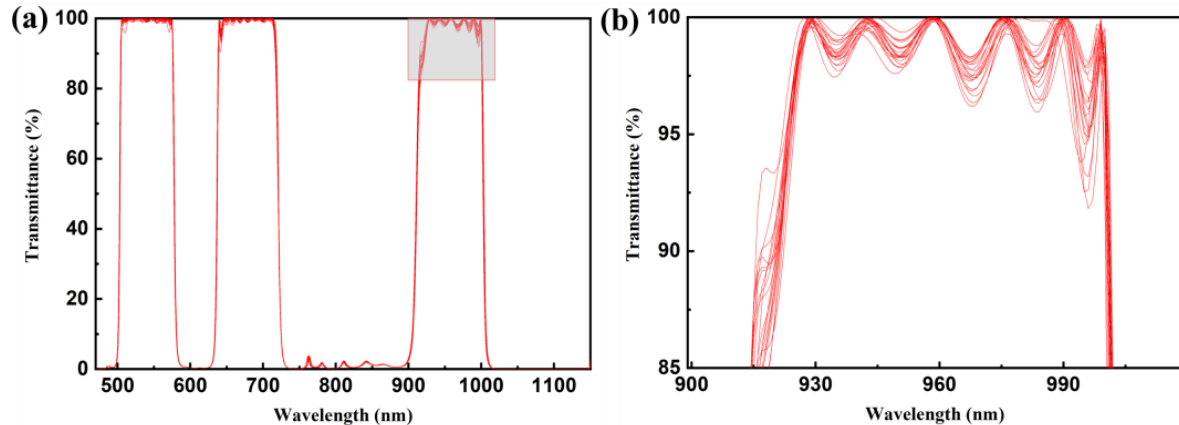


Figure 4. (a) Simulation curve with 3‰ random error. (b) Partially enlarged drawing of the 900~1020 nm region.

3. Thin Film Preparation and Analysis

3.1. Temperature Gradient in the Material

The preparation temperature of the film affects the optical constants and surface roughness of the material [32]. By analyzing the changes in the optical parameters and surface roughness of Ta₂O₅ at different temperatures, an appropriate process was selected for the preparation of the filter. Since SiO₂ material is less affected by environmental changes, the preparation parameters were determined by analyzing the surface roughness of Ta₂O₅ with a high refractive index. The method of electron beam deposition was used for the experiment via a Leybold SYRUSpro1110 coating machine. The deposition rate of Ta₂O₅ was 0.3 nm/s. Figure 5a shows the optical constants of the film at deposition temperatures of 120 °C, 150 °C, 180 °C, 210 °C, and 240 °C, with a deposition thickness of 500 nm. Figure 5b shows the surface roughness of the film at different temperatures.

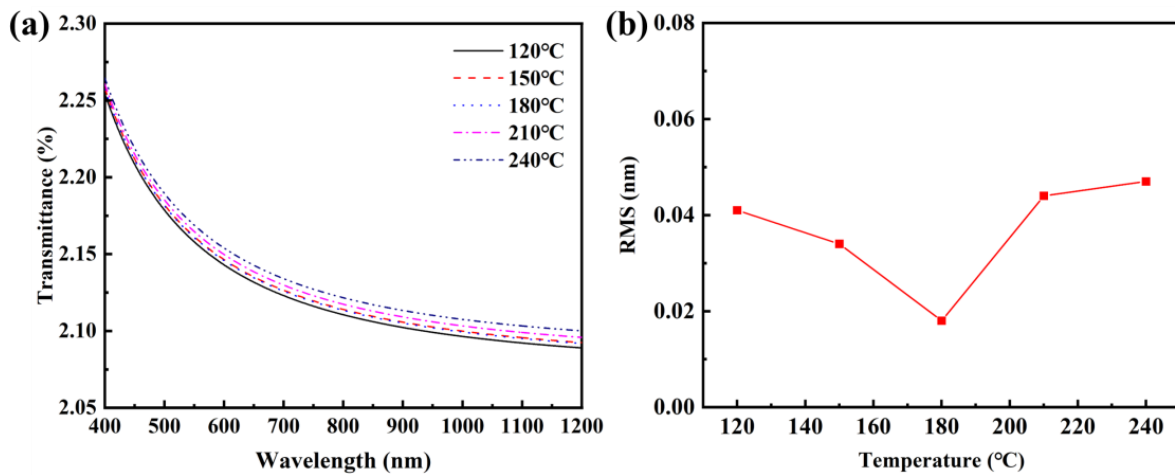


Figure 5. (a) The refractive index of Ta₂O₅ at different temperatures. (b) The surface roughness of Ta₂O₅ thin films at different temperatures.

Testing results indicate that the refractive index of Ta₂O₅ increases with a rise in substrate temperature, while surface roughness decreases first and then increases with a rise in the substrate temperature. Based on the principles of thin film dynamics [33,34], substrate temperature affects the ability of atoms to migrate on the growing surface. At lower substrate temperatures, the ability of atoms to migrate is weak. With an increase in substrate temperature, the migration of adsorbed atoms becomes more active, leading to a decrease in surface roughness. However, when the substrate temperature reaches a certain level, atoms begin to jump from low to high rough positions, resulting in an increase in surface roughness with temperature. This roughness affects the propagation of light, leading to light loss. Taking all factors into consideration, a deposition temperature of 180 °C was chosen for the final preparation of the multi-bandpass filter.

3.2. Preparation of Multi-Bandpass Filter

The Leybold SYRUSpro1110 coating machine was used to prepare the multi-bandpass filter. The experimental temperature was determined as 180 °C based on the temperature gradient, and the background vacuum degree was 1.0×10^{-3} Pa. The deposition rates of Ta₂O₅ and SiO₂ were 0.3 nm/s and 0.7 nm/s, respectively. The deposition process parameters are shown in Table 3. We adapted the optimized film structure from Section 2.2.

Table 3. Deposition process parameters of Ta₂O₅ and SiO₂.

Material	Substrate Temperature/°C	Degree of Vacuum/Pa	Deposition Rate/nm·s ⁻¹	Flow Rate of O ₂ /sccm	
				APS	HPE
Ta ₂ O ₅	180	1×10^{-4}	0.30	35	15
SiO ₂	180	1×10^{-4}	0.70	25	25

3.3. Filter Testing

3.3.1. Spectral Testing

The multi-bandpass filter prepared was spectrally tested using an Agilent Cary 7000 spectrophotometer, and the spectral testing results are shown in Figure 6.

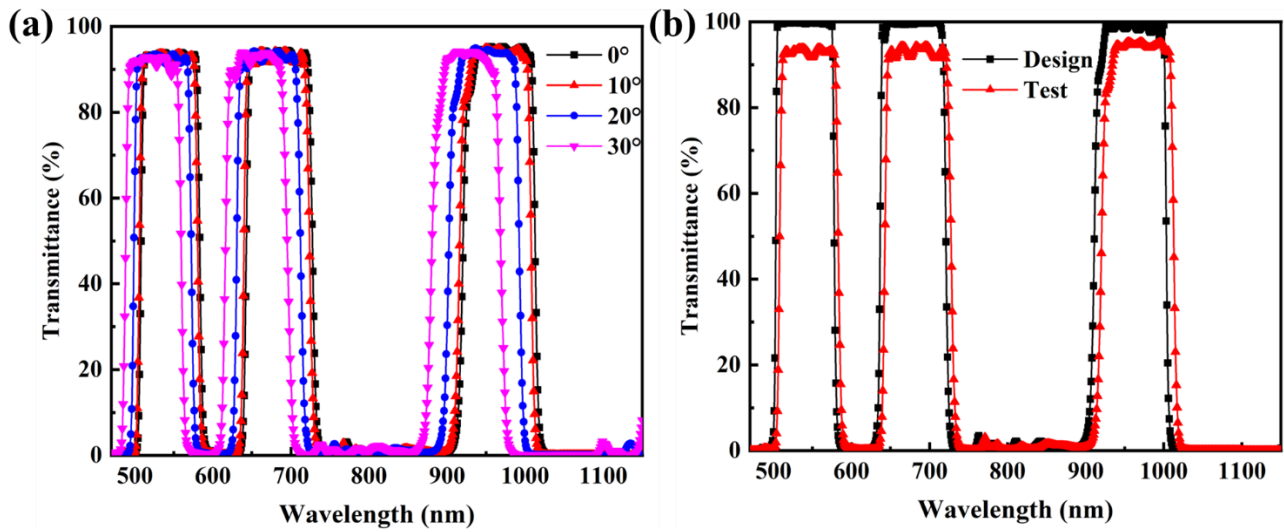


Figure 6. (a) Transmittance test curve of 0°~30° multi-bandpass filter. (b) Design transmittance curve and test transmittance curve of 0°-incident-angle multi-bandpass filter.

The average transmittance under 0°, 10°, 20° and 30° conditions are shown in Table 4. Through analysis, the difference between measured transmittance and theoretical transmittance was found to be caused by deposition thickness errors. However, the impact of these errors was minimal, and the final experimental data meet the design requirements.

Table 4. Test results of multi-bandpass filter.

Incident Angle	Wavelength/nm	Average Transmittance/%
0°	515~545	93.33
	645~675	92.42
	925~955	91.38
10°	515~545	93.03
	645~675	92.83
	925~955	92.53
20°	515~545	92.76
	645~675	93.09
	925~955	94.24
30°	515~545	91.98
	645~675	92.94
	925~955	92.99

3.3.2. Roughness Testing

Surface roughness affects the quality of thin films directly. A higher surface roughness can lead to defects and impurities in the thin film, reducing its crystallinity and compactness. Higher surface roughness can increase light scattering, thus affecting the transparency and optical properties of the thin film. Using the Zygo Verifire interferometer for surface roughness testing, the test results are shown in Figure 7, with a peak valley (PV) value of 0.374 and a root mean square (RMS) value of 0.05 nm, which meet the technical specifications.

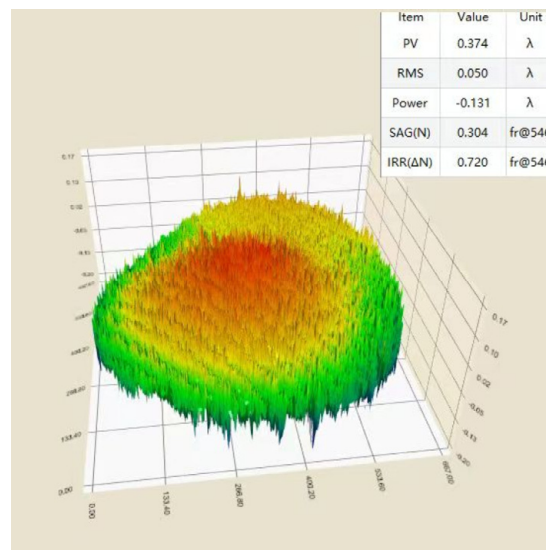


Figure 7. Surface roughness test chart.

3.3.3. Weak Absorption Test

Using the Stanford hot–lens weak–absorption spectrometer, the weak absorption of the film was measured. The test results are shown in Figure 8. The weak absorption of the multi–bandpass filter produced was about 139 ppm. The result indicates that the filter has minimal absorption, which does not affect the spectral transmittance and light utilization efficiency, thus meeting the requirements for use.

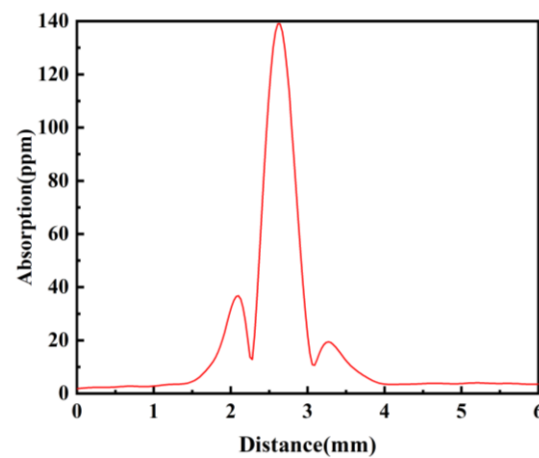


Figure 8. Measured weak absorption results.

3.3.4. SEM Test

The multi–segment bandpass filter prepared was tested using a scanning electron microscope with a resolution of 1 μm. The test results, as shown in Figure 9, indicate that the deviation between the actual thickness of the multilayer films and the theoretical thickness is less than 0.5%. From Figure 9, the multilayer film stack can be clearly seen. The film has a high–quality structure without defects.

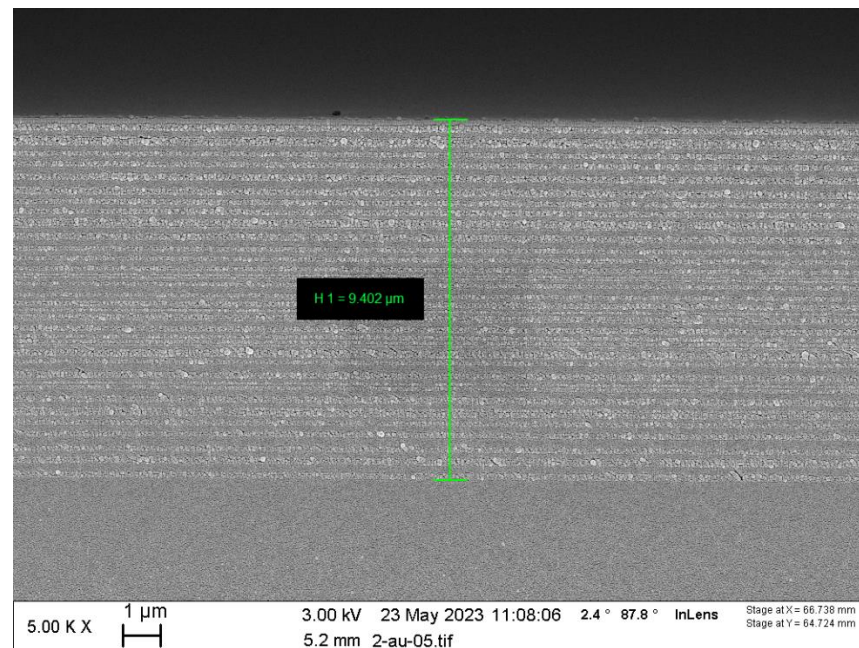


Figure 9. Multilayer thin–film SEM spectroscopy.

4. Conclusions

In this paper, we present an enhanced design of an F–P narrowband filter by increasing the interference order and incorporating a new series–connected F–P structure, which expands the spectral range of the multi–bandpass filter. We have successfully developed a multi–bandpass filter characterized by a wide half–wave and cutoff, meeting the necessary requirements. This advanced filter has been implemented in smart wearable devices, offering multi–angle adaptability that eliminates monitoring limitations due to human body movements. Its exceptional spectral filtering properties enable the accurate and real–time monitoring of physiological parameters under various complex backgrounds, thus minimizing the impact of external environmental factors on detection accuracy.

The multi–bandpass filter significantly improves the visual performance of smart wearable devices. In health monitoring applications, it delivers more precise and comprehensive health monitoring while providing personalized services. As a result, it facilitates earlier disease prediction and ultimately enhances users’ quality of life. In future research, we will investigate the filter’s potential applications in other domains, such as medical imaging and wireless communication. Further advancements in multi–bandpass filter research will bolster spectral filtering capabilities, which hold significant promise for the development of sensors in smart wearable devices.

Author Contributions: Conceptualization, H.J. and D.C.; methodology, H.J.; validation, Y.J., H.J., R.F. and K.G.; formal analysis, H.J., S.X. and D.C.; investigation, R.F., Y.J. and C.Z.; data curation, X.W. and C.Z.; resources, S.X. and B.S.; software, X.W.; writing—original draft preparation, H.J.; writing—review and editing, D.C., S.X., K.G. and B.S.; visualization, H.J. All authors have read and agreed to the published version of the manuscript.

Funding: This work is supported by the National Natural Science Foundation of China (62193277012).

Institutional Review Board Statement: Not applicable.

Informed Consent Statement: Not applicable.

Data Availability Statement: The data used in this research are available from the corresponding author upon reasonable request.

Conflicts of Interest: Bing Sun is affiliated to China Electronics Technology Group Corporation. The remaining authors declare that there is no conflict of interest.

Abbreviations

List of symbols

B	Magnetic induction intensity vector
C	Magnetic field intensity vector
φ	Phase difference
δ	Phase of the film
λ	Wavelength of electromagnetic wave

Abbreviations

PPG	Photoplethysmography
PD	Photodiode
LED	Light-emitting diode
F–P	Fabry–Perot
PV	Peak valley
RMS	Root mean square

References

1. Keshet, A.; Reicher, L.; Bar, N.; Segal, E. Wearable and digital devices to monitor and treat metabolic diseases. *Nat. Metab.* **2023**, *5*, 563–571. [[CrossRef](#)]
2. Han, M.; Lee, Y.R.; Park, T.; Ihm, S.H.; Pyun, W.B.; Burkard, T.; Cho, M.C.; Camafort, M.; Yang, E.; Stergiou, G.S.; et al. Feasibility and measurement stability of smartwatch-based cuffless blood pressure monitoring: A real-world prospective observational study. *Hypertens. Res.* **2023**, *46*, 922–931. [[CrossRef](#)]
3. Ates, H.C.; Nguyen, P.Q.; Gonzalez–Macia, L.; Morales–Narváez, E.; Güder, F.; Collins, J.J.; Dincer, C. End-to-end design of wearable sensors. *Nat. Rev. Mater.* **2022**, *7*, 887–907. [[CrossRef](#)]
4. Kamshilin, A.A.; Nippolainen, E.; Sidorov, I.S.; Vasilev, P.V.; Erofeev, N.P.; Podolian, N.P.; Romashko, R.V. A new look at the essence of the imaging photoplethysmography. *Sci. Rep.* **2015**, *5*, 10494. [[CrossRef](#)]
5. Bashar, S.K.; Han, D.; Hajeb–Mohammadalipour, S.; Ding, E.; Whitcomb, C.; McManus, D.D.; Chon, K.H. Atrial fibrillation detection from wrist photoplethysmography signals using smartwatches. *Sci. Rep.* **2019**, *9*, 15054. [[CrossRef](#)]
6. Viciano–Tudela, S.; Sendra, S.; Lloret, J.; Tomas, J.; Belda–Ramirez, J. Development of a Low-Cost Pulse Oximeter for Taking Medical–Scientific Parameters to Monitor Remote Patients. *Electronics* **2022**, *11*, 3061. [[CrossRef](#)]
7. Elgendi, M.; Fletcher, R.; Liang, Y.; Howard, N.; Lovell, N.H.; Abbott, D.; Lim, K.; Ward, R. The use of photoplethysmography for assessing hypertension. *NPJ Digit. Med.* **2019**, *2*, 60. [[CrossRef](#)]
8. Lee, H.S.; Noh, B.; Kong, S.U.; Hwang, Y.H.; Cho, H.E.; Jeon, Y.; Choi, K.C. Fiber-based quantum-dot pulse oximetry for wearable health monitoring with high wavelength selectivity and photoplethysmogram sensitivity. *NPJ Flex. Electron.* **2023**, *7*, 15. [[CrossRef](#)]
9. Sharma, D.; Kaur, R.; Singh, G. A Comparative Analysis of Adaptive IIR Filtering Techniques using LabVIEW. *Int. J. Hyb. Info. Tech.* **2015**, *8*, 289–302. [[CrossRef](#)]
10. Peng, F.; Liu, H.; Wang, W. A comb filterbased signal processing method to effectively reduce motion artifacts from photoplethysmographic signals. *Physiol. Meas.* **2015**, *36*, 2159. [[CrossRef](#)]
11. Liang, Y.; Elgendi, M.; Chen, Z.; Ward, R. An optimal filter for short photoplethysmogram signals. *Sci. Data* **2018**, *5*, 180076. [[CrossRef](#)]
12. Ahmed, R.; Mehmood, A.; Rahman, M.M.U.; Dobre, O.A. A Deep Learning & Fast Wavelet Transform-based Hybrid Approach for Denoising of PPG Signals. *IEEE Sens. Lett.* **2023**, *2301*, 6549.
13. Macleod, H.A. *Thin-Film Optical Filters*, 4th ed.; CRC Press: Boca Raton, FL, USA; Taylor & Francis: Abingdon, UK, 2010.
14. Wang, L.; Wang, Z.; Wu, Y.; Chen, L. Design of multi-channel filters based on Fabry Perot structure. *Opt. Precis. Eng.* **2003**, *11*, 643–646.
15. Wang, S.; Chen, X.; Lu, W.; Wang, L.; Wu, Y.; Wang, Z. Integrated optical filter array fabricated by using the combinatorial etching technique. *Opt. Lett.* **2006**, *31*, 332–334. [[CrossRef](#)]
16. Kamikawa, S. How to design an easily deposited multi-band-pass filter. *Passiv. Compon. Fiber-Based Devices V SPIE* **2008**, *7134*, 686–693.
17. Zhao, S.; Lv, S.; Wang, R.; Jiang, C.; Hu, W.; Li, M. Design and manufacture of PCR dual-band-pass optical filter based on PARMS coating technology & plant. *Vacuum* **2018**, *55*, 4.
18. Zhu, Y. Design of three-channel filter based on F–P filter. *Vacuum* **2019**, *5*, 74–76.
19. Chen, G.; Liu, D.; Ma, C.; Wang, K.; Zhang, L.; Gao, L. Spectrum modulation of a thin-film filter with visible and near infrared dual bandpass channel. *J. Infrared Millim. Waves* **2020**, *39*, 791–795.
20. Zhou, S.; Zhang, L.; Guo, F.; Wu, C.; Xu, J.; Zhang, K.; Li, K.; Liu, Z.; Xiao, X.; Song, S.; et al. Design and fabrication of an integrated dual-channel thin-film filter for the mid-infrared. *Coatings* **2021**, *11*, 803. [[CrossRef](#)]
21. Ren, S.; Gao, P.; Zhao, S.; Wang, R.; Wang, Z.; Ban, C. Design of Coating System for Multi-pass Filter in Fluorescence Application. *Vacuum* **2020**, *57*, 14–18.

22. Qi, L.; Xu, B.; Wang, Y. A 3D projection system based on complementary multiband bandpass filter. *Opto–Electron. Eng.* **2020**, *47*, 190334.
23. Wang, Z.; Sang, T.; Wang, L.; Zhu, J.; Wu, Y.; Chen, L. Guided–mode resonance Brewster filters with multiple channels. *Appl. Phys. Lett.* **2006**, *88*, 251115. [[CrossRef](#)]
24. Hao, Q.; Fu, X.; Song, S.; Gibson, D.; Li, C.; Chu, H.; Shi, Y. Investigation of TiO₂ Thin Film Deposited by Microwave Plasma Assisted Sputtering and Its Application in 3D Glasses. *Coatings* **2018**, *8*, 270. [[CrossRef](#)]
25. Fu, X.; He, S.; Jia, X.; Liu, D.; Zhang, J.; Liu, S. Study and Fabrication of the Dual Band–pass in Grain Screening System. *Acta Photonica Sin.* **2014**, *43*, 1216001.
26. Bekshaev, A.Y.; Grimblatov, V.M.; Okunisnikov, O.N.; Petrenko, R.A.; Koverznev, V.N. Spectral characteristics of the Fabry–Perot interferometer transmission upon illumination by an arbitrary light beam. *arXiv* **2018**, arXiv:1812.11687.
27. Friedrich, K.; Wilbrandt, S.; Stenzel, O.; Kaiser, N.; Hoffmann, K.H. Computational manufacturing of optical interference coatings: Method, simulation results, and comparison with experiment. *Appl. Opt.* **2010**, *49*, 3150–3162. [[CrossRef](#)]
28. Shang, P.; Xiong, S.; Li, L.; Tian, D.; Ai, W. Investigation on thermal stability of Ta₂O₅, TiO₂ and Al₂O₃ coatings for application at high temperature. *Appl. Surf. Sci.* **2013**, *285*, 713–720. [[CrossRef](#)]
29. Kumar, M.; Kumari, N.; Kumar, V.P.; Karar, V.; Sharma, A.L. Determination of optical constants of tantalum oxide thin film deposited by electron beam evaporation. *Mater. Today Proc.* **2018**, *5*, 3764–3769. [[CrossRef](#)]
30. Zhang, J.; Wang, M.; Geng, H.; Shi, C.; Sun, Y. Design and Preparation Technology of 3D Eyeglasses Optical Thin Film. *Electro–Opt. Technol. Appl.* **2018**, *33*, 39–43.
31. Guo, X.; Quan, X.; Li, Z.; Li, Q.; Zhang, B.; Zhang, X.; Song, C. Broadband anti–reflection coatings fabricated by precise time–controlled and oblique–angle deposition methods. *Coatings* **2021**, *11*, 492. [[CrossRef](#)]
32. Al–Ghamdi, S.A.; Darwish, A.A.A.; Hamdalla, T.A.; Alzahrani, A.O.M.; Khasim, S.; Qashou, S.I.; Abd El–Rahman, K.F. Preparation of TlInSe₂ thin films using substrate temperature: Characterization, optical and electrical properties. *Opt. Mater.* **2022**, *129*, 112514. [[CrossRef](#)]
33. Merkh, T.; Spivey, R.; Lu, T.M. Time invariant surface roughness evolution during atmospheric pressure thin film depositions. *Sci. Rep.* **2016**, *6*, 19888. [[CrossRef](#)] [[PubMed](#)]
34. Kilic, U.; Mock, A.; Sekora, D.; Gilbert, S.; Valloppilly, S.; Melendez, G.; Ianno, N.; Langell, M.; Schubert, E.; Schubert, M. Precursor–surface interactions revealed during plasma–enhanced atomic layer deposition of metal oxide thin films by in–situ spectroscopic ellipsometry. *Sci. Rep.* **2020**, *10*, 10392. [[CrossRef](#)] [[PubMed](#)]

Disclaimer/Publisher’s Note: The statements, opinions and data contained in all publications are solely those of the individual author(s) and contributor(s) and not of MDPI and/or the editor(s). MDPI and/or the editor(s) disclaim responsibility for any injury to people or property resulting from any ideas, methods, instructions or products referred to in the content.